Journal of Petroleum Science and Engineering 208 (2022) 109769

Contents lists available at ScienceDirect

Journal of Petroleum Science and Engineering

journal homepage: www.elsevier.com/locate/petrol

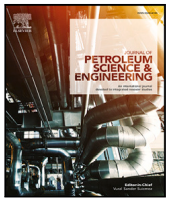

Effects of confinement pressure on the mechanical behavior of an oil well cement paste

Victor Nogueira Lima [a], Flávio de Andrade Silva [a], Hans Joakim Skadsem [b,c,*], Katherine Beltrán-Jiménez [b,c], Jonas Kristoffer Sunde [c]

[a] Pontifícia Universidade Católica do Rio de Janeiro (PUC-Rio), Rua Marquês de São Vicente 225, 22451-900 Rio de Janeiro, Brazil
[b] University of Stavanger, P.O. Box 8600, 4036 Stavanger, Norway
[c] Norwegian Research Centre AS, P.O. Box 8046, 4068 Stavanger, Norway

ARTICLE INFO

Keywords:
Cement
Zonal isolation
Triaxial testing

ABSTRACT

Oil well cement paste is a key structural component in wells that should provide mechanical support to the casing and prevent uncontrolled flow of formation fluids along the wellbore and to the environment. Since the annular cement paste is subjected to both hydrostatic pressure and to loads from formation or through the casing, it is important to understand the mechanical behavior and strength of oil well cement pastes under confining conditions. We study cement specimens cored from test sections that were cemented using a full-scale batch mixer. The specimens were tested mechanically without confinement and under 10, 20 and 40 MPa confining pressures using a state of the art triaxial test system. Unconfined samples are found to exhibit linear elastic behavior up to axial strains of approximately 0.2% with an average Young's modulus of 14.9 GPa and a Poisson ratio of 0.21. At larger strains, the stress–strain response deviates from the initial slope, terminating with a brittle shear failure at axial strains of approximately 0.5%. The corresponding average uniaxial compressive strength is 58 MPa, in good agreement with previously published results. When subjected to confining pressures of 10 MPa or higher, the cement paste accommodated larger strains at a given level of deviatoric stress, and maintained its load-carrying capacity through the entire test cycle. The Young's modulus for the initial loading phase was found to decrease with increasing confining pressures, and the ultimate deviatoric stress approached approximately 80 MPa, independent of the magnitude of the confining pressures used in this study. The results suggest that the main effect of increasing confining pressure is to increase the sample ductility and the axial strain corresponding to the ultimate deviatoric stress. It is further found that the confined stress–strain behavior of the oil well cement paste can be described by a simple nonlinear constitutive equation. The more ductile and flexible response of well cement under relevant confining pressures is considered to be a positive characteristic of cement as a barrier material for zonal isolation. This study is based on a commercial well cement slurry that is mixed and placed using field equipment. The results are therefore considered novel and unique, and can contribute toward improved knowledge and evaluation of mechanical well cement behavior under realistic, confined conditions.

1. Introduction

The cement paste behind casings is an important structural barrier element in wells for oil and gas production that should ensure zonal isolation along the annulus and provide mechanical support to the casing (Nelson and Guillot, 2006). The cement paste is usually placed behind the casing or liner by pumping a sequence of fluids, including washing fluids, spacer fluids and the cement slurry, down the well inside the casing (Nelson and Guillot, 2006; Bittleston and Guillot, 1991; Bittleston et al., 2002). The fluids flow into the annulus behind the casing and up toward the surface, displacing the original drilling fluid from the annular space. Once in place, the cement slurry gradually and irreversibly hardens into a solid and low-permeable annular cement sheath that occupies the narrow and confined space between casing and formation wall, or between successive casing strings of different diameter. During its lifetime, the well cement paste is subjected to hydrostatic pressure as well as mechanical loads due to *e.g.* pressure- or mechanically induced casing expansion, or stress changes in the overburden due to production or fluid injection. In order to assess the long-term integrity of oil well cement pastes, it is therefore important

* Corresponding author at: University of Stavanger, P.O. Box 8600, 4036 Stavanger, Norway.
E-mail address: hans.j.skadsem@uis.no (H.J. Skadsem).

https://doi.org/10.1016/j.petrol.2021.109769
Received 14 July 2021; Received in revised form 1 October 2021; Accepted 29 October 2021
Available online 11 November 2021

to understand the mechanical properties and strength of cement pastes under relevant confined conditions (Palou et al., 2014; Le Saout et al., 2006; Arjomand and Bennett, 2018).

Well cement pastes generally exhibit brittle mechanical response when compressed under unconfined conditions, and normally fail abruptly at the unconfined compressive strength (UCS) (Nelson and Guillot, 2006). The stress–strain behavior is well characterized by linear elasticity with a Young's modulus of the order of 1–20 GPa, and a Poisson ratio of about 0.2. In the presence of confining pressure, such as the hydrostatic pressure in a well, it is well-known that cement pastes behave more ductile, often exhibiting strain hardening and increasing compressive strengths (Nelson and Guillot, 2006; Handin, 1965; Sakai et al., 2016). Hardened cement is also a porous material that is considered to exhibit poroelastic behavior (Nelson and Guillot, 2006; Ghabezloo et al., 2008). According to Jennings et al. (2002), hardened cement can possess more than 25% porosity, with pore sizes spanning from gel pores at the nanometer scale to capillary pores at the micrometer scale and voids at even larger length scales. The highly heterogeneous microstructural character of cementitious materials certainly presents key challenges for accurately describing their mechanical performance, including: yield criteria, plastic behavior, failure criteria, as well as underlying failure mechanisms (Eseme et al., 2007; Bourissai et al., 2013).

Among the first to perform detailed triaxial testing of cement pastes and sedimentary rocks under simulated downhole conditions was Handin (1965), Handin and Hager (1957, 1958) and Handin et al. (1963). These studies included variations in confining pressure, pore pressure, and temperature, using siltstone, shale, sandstone, limestone, dolomite rock, anhydrite, and salt rock (halite) in addition to cement pastes. Generally, marked increases in strength and ability to deform permanently without fracturing were found with increasing confinement pressure for all materials tested. Increased pore pressure and/or temperature generally lead to lower strength. A wide range of oil well cement pastes were tested up to an effective pressure (difference between external and internal sample pressure) of 103 MPa (Handin, 1965). A near linear relationship was found between the ultimate compressive strength and the effective confining pressure, σ_3, of the form $\sigma_1 = a + b\sigma_3$, where a is the UCS and b an empirical constant (≈ 2). Significant ductile behavior (strains larger than 0.2) was obtained already at approximately 21 MPa effective confining pressure. The UCS of the different cement types measured $\lessapprox$ 66 MPa, and at $\sigma_3 = 103$ MPa the ultimate strengths ranged from approximately 207–345 MPa, being comparable to the strength of relevant sedimentary rocks under similar pressure conditions (Handin, 1965). The tests were conducted using a strain rate, $\dot{\epsilon} = 1.67 \cdot 10^{-4}$ s^{-1}, and with an effective pore pressure of 0 as excess fluid was allowed to escape the system (drained condition). Without an escape path for free water (undrained condition), confinementment exerted no effect on the cement paste strength, and no work-hardening was observed. This occurred as the pore pressure rapidly approached the value of the external confining pressure due to compaction of the pore space volume.

A linear relationship between ultimate strength and confining pressure was found also by Thiercelin et al. (1998) ($b \approx 1.6$), who studied shrinkage of neat Class G cement pastes under triaxial testing using confining pressures of 0, 10 and 30 MPa, and a loading rate of $\dot{\epsilon} =$ 0.025 mm/min and 0.0075 mm/min. By regarding cement paste as a weakly-bonded porous solid, the test results were used to calibrate a Cam-Clay model for predicting cement paste shrinkage. This soil mechanics approach showed that the strength increase of cement paste can be linked to a compaction mechanism that occurs under increasing mean effective stress.

Sakai et al. (2016) tested ordinary Portland cement pastes (OPC) with initial porosity of 18% under very high confining pressures, including 30, 100 and 400 MPa. A similar strain-hardening slope was found in the deviatoric stress vs. axial strain plot for all confining pressures tested. Ductility and peak strength increased with confining pressure, but no systematic relationship was found. It was therefore suggested that the ductile strength of the cement paste was limited by crystal plasticity, rather than frictional cataclastic flow under high confinement pressures (Sakai et al., 2016).

More recently, Jimenez et al. (2019) studied the mechanical integrity of well cement pastes under *in-situ* conditions using a novel experimental setup. Young's modulus and compressive strength were reported for 1917 kg/m^3 cement slurries cured at 27 °C and 177 °C, and σ_3 ranging from 20 to 55 MPa. Measurements indicated a fairly constant Young's modulus of approximately 10 GPa, and a weak increase in the compressive strength of the samples with increasing curing and confining pressure. Fitting measurements to the Mohr–Coulomb shear failure criterion suggested a cohesive strength of approximately 14 MPa and a low friction angle of $\phi = 4.9°$ (Jimenez et al., 2019). The low friction angle suggests a weak increase in deviatoric strength with increasing confining pressure.

Numerical models can be used to predict the integrity of well cement pastes under downhole conditions where a fairly complex stress state can exist within the annulus cement sheath (Bois et al., 2011; Patel and Salehi, 2019). To support such studies, empirical models of cement paste stress–strain behavior under varying confining pressures are developed based on triaxial testing of well cement paste. Li et al. (2019) recently proposed a new stress–strain model encompassing both uniaxial and triaxial test data. Their experiments utilized Class G cement pastes with various additives and tests were conducted up to 20 MPa confining pressure. The stress–strain response of a compressive confinement test was modeled in three stages, from an initial parabolic loading phase up to the peak stress, to a plateau at the peak level followed by a descending, post-peak softening stage. The experimental results presented by Li et al. (2019) suggest an increasing ultimate strength as the confining pressure increases. Typical uniaxial compressive strengths are of the order of 60 MPa with an abrupt and sudden failure at the peak stress level. At confining pressures of 10 MPa and 20 MPa, the ultimate strength increases upward to 80–100 MPa (Li et al., 2019).

The fact that confined cement paste can withstand significant plastic deformation is a mechanism that is utilized by casing expansion technologies to close migration paths behind casing (Kupresan et al., 2014; Du et al., 2015; Radonjic et al., 2015; Wolterbeek et al., 2021). In the study by Kupresan et al. (2014), the effectiveness of casing expansion was investigated in short annulus sections consisting of 2 3/8-in pipes cemented inside 4-in pipes. The cemented annulus had initial permeabilities ranging from 0.1 to 10 darcy. The annulus was subsequently compressed radially by using an expansion cone to expand the diameter of the inner pipe by 2 to 8%. The casing expansion was found to reduce the permeability by several orders of magnitude, and inspection of the compressed annulus cement suggested compaction due to pore collapse, displacement of pore fluid, and an apparent softening and rehydration of the cement (Kupresan et al., 2014). More recently, a tool has been developed that performs *local* casing expansion by pressing hardened steel fingers into the wall of the inner casing (Cornelissen, 2019). Extensive laboratory studies of casing expansion indicated densification of the cement paste and formation of cohesive shear bands as a result of the local expansion (Wolterbeek et al., 2021).

As suggested by the literature review above, hydrated cement paste is a highly complex material and several of its microstructural properties are still in the process of being explored. The purpose of the present study is to investigate the effects of confinement on the mechanical behavior of cement samples cored from test sections that were cemented using a field cement batch mixer. The focus of the research is on the stress–strain response at different confining pressures up to 40 MPa, and to study the transition from brittle to predominantly plastic yielding as the confining pressure increases. The outline of the paper is as follows. We begin by summarizing the original cementing operation, the cement slurry properties and the curing conditions in Section 2. We present the coring program and subsequent characterization of core

Table 1
Cement slurry composition.

Ingredient	Quantity
Class G cement	100 kg/100 kg
KCl brine	37.28 l/100 kg
Fluid loss additives	4.5 l/100 kg
Free water control additive	3.5 l/100 kg
Retarder	1 l/100 kg
Defoamer	0.1 l/100 kg

plugs in Sections 3 and 4, respectively. The mechanical measurements are detailed in Section 5 followed by a presentation of the results obtained from uniaxial strength tests and the triaxial test program in Sections 6.1 and 6.2, respectively. Measurements of stress and strain under confined conditions are fitted to a nonlinear constitutive model in Section 7. Finally, we end the paper by summarizing the main results and provide our conclusion.

2. Cementing operation

The cement paste samples used in this study were cored from casing-annulus test sections that were cemented in November 2017 as part of a full-scale fluid displacement and cementing experiment. The main purpose of these experiments was to study the cement slurry placement process, and possible effects of sudden hole enlargements on the hydrated cement paste quality. Cementing was performed using a conventional Class G cement paste with standard additives such as retarder, defoamer and stabilizer. After cementing and curing, the cement quality was probed by a series of pressure and flow tests, followed by dissection of the sections into shorter segments. Several hydrated cement paste cores were retrieved from these test sections in 2020 and 2021 for the present triaxial strength testing of oil well cement pastes. A summary of the cementing operation and curing is provided below and additional details are given by Skadsem et al. (2019).

Cementing experiments were performed in a total of four annulus test sections that were constructed at Ullrigg Test Centre in 2017. The test sections consisted of two joints 7-in (177.8 mm) tubing placed inside 9 5/8-in (244.5 mm) casing. The assemblies were inclined to 85° from the vertical, resulting in near-horizontal cementing conditions. An overhead view of the test sections prior to cementing is provided in Fig. 1. The assemblies were wrapped in wool insulation and draped in plastic to provide protection from ambient temperature variations and to retain some of the heat generated by the curing process.

Two fluids were used as part of the cementing experiments: A water-based spacer fluid consisting of a polymeric viscosifier and barite as weighting material, and a conventional class G cement slurry. The fluids were injected into the test assemblies by feeding fluid from the mixing compartments in the batch mixer to one of the mud pumps at Ullrigg Test Centre. A wiper ball was mounted inside the 7-in tubing and ensured physical separation of the spacer and the cement slurry during injection inside the tubing. Cement slurry was injected into the relevant sections at a constant rate of 800 l/min. At the end of the injection phase, the inner tubing and the annulus between tubing and casing were filled with cement slurry.

The cement slurry recipe is provided in Table 1. As indicated in the table, a KCl brine was used for the mixing water. The salt concentration corresponded to 3% KCl by weight of cement slurry. The motivation for adding salt to the mixing water was to use the electrical conductivity of the cement slurry as a marker for monitoring the spacer displacement and cement placement using conductivity probes mounted at designated positions along the test sections, and at the outlet. The cement slurry was mixed at the site of the cementing experiments using a standard offshore type batch mixer with 2 mixing compartments, each with capacity of 8 m^3 fluid. The cement slurry

Fig. 1. View of the four test assemblies draped in insulation and plastic covers.

was mixed in one of the compartments, while the spacer fluid was agitated in the second compartment. The mass density and viscosity of the cement slurry were measured by sampling the slurry from the mixing tank. The mass density was measured to be 1910 kg/m^3 using a mud balance, while the viscosity was measured with a standard Fann 35 viscometer. These measurements are shown in Fig. 2. Also shown in the figure is a Bingham plastic model, $\tau = \tau_y + \mu_p\dot{\gamma}$, with τ denoting the shear stress and $\dot{\gamma}$ the shear rate. A least squares fitting to the Fann 35 measurements gave a yield stress $\tau_y = 1.4$ Pa and a plastic viscosity $\mu_p = 0.15$ Pa s. The coefficient of determination, R^2, is larger than 0.99 for this parametrization, suggesting good agreement between the two-parameter model and the measurements. The relatively small yield stress implies that the slurry was predominantly viscous with only minor viscoplastic behavior.

Once injection was complete, the assemblies were connected to the water main source, and cured under approximately 6 bar water pressure. The exothermic reaction in the cement ensured elevated curing temperature for several days. The maximum curing temperature measured at the exterior of the outer casing and underneath the insulation was close to 70 °C, more than 60 °C above the average ambient temperature; this maximum temperature was measured approximately 30.5 h after cementing (Skadsem et al., 2019). The temperature decreased gradually over the following days, reaching 40 °C approximately 80 h after cementing. In all, the assemblies were allowed to cure for 7 days before a series of pressure and flow tests were performed to measure the permeability of the cemented annuli. The assemblies were then sectioned into shorter segments that have been stored outside for 2 years prior to extracting cores from the cement inside the tubing. The segments were stored unprotected and exposed to the local weather conditions during these years in storage, *i.e.* both cold (freezing) conditions during winter time and warmer (> 20 °C) periods during the summer months.

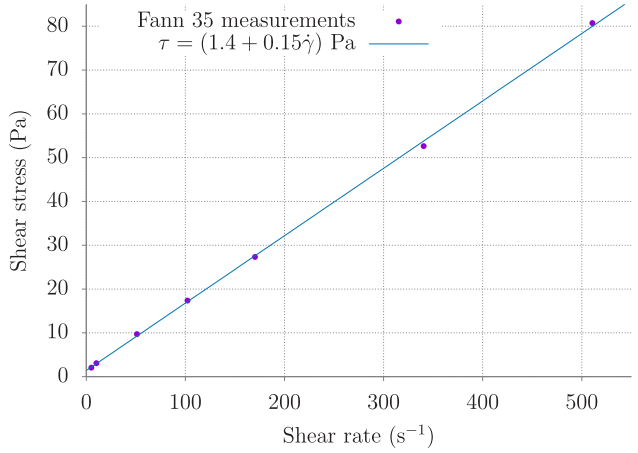

Fig. 2. Fann 35 measurements of the cement slurry prior to injection into the test assemblies. The solid line is the corresponding Bingham plastic fit to the measurements.

Fig. 3. Specimen preparation process: (a) Coring of cement samples and (b) sizes of cores recovered for testing.

3. Coring program

Cores for this study were cut from one of the shorter segments mentioned in the previous section, using coring bits of either 2-in (50.8 mm) or 1.5-in (38.1 mm) bit diameter. As shown in Fig. 3a, cores were drilled from the hydrated cement paste inside the 7-in (177.8 mm) tubing.

The nomenclature used for identification of cores is of the form X-CPY, where X denotes the axial position the core was retrieved from. The second identifier, Y, denotes the order in which the cores from the given section were cut (*i.e.* 1 being the first core cut from the given axial position). Table 2 present an overview of the cores, their dimensions and the mechanical measurements performed on each sample. The coring was performed in November 2019. Three additional cores, 9-CPY, were cut in 2020 specifically for micro-computed tomography analysis, reported in Section 4.2.

Additional cement material that was collected during the coring program was used for chemical characterization of the cement using thermogravimetric analysis (TGA) and X-ray diffraction (XRD). The TGA was performed using a 10 mg cement sample. The test was performed in nitrogen atmosphere, starting with a constant temperature of 35 °C for 60 min, followed by a gradual temperature increase up to 1000 °C at a rate of 10 °C per minute. Measurements of the sample weight percent as function of temperature (TG) and the change in weight percent per unit time, or first derivative (DTG) are presented in Fig. 4. The measurements show that the main phases of cement are calcium sulfate (C-S-H) and portlandite. The calcite content of 0.62% in the sample suggests that only minor chemical degradation may have occurred within the material. XRD measurements were performed for deflection angles 2θ between 8° and 90° with the detector

Table 2
Physical dimensions and confining pressure conditions for strength measurements. All listed cores were also subject to measurement of ultrasonic p-wave velocity measurement.

Core	Length (mm)	Diameter (mm)	Testing conditions	
			Unconfined	Confined
1-CP1	100.1	50.0		10 MPa
1-CP2	100.0	50.0		40 MPa
2-CP1	99.9	50.0		10 MPa
3-CP1	99.9	50.1		10 MPa
4-CP1	99.9	50.1	✓	
4-CP2	99.9	50.2		20 MPa
5-CP1	100.6	50.2	✓	
5-CP2	100.4	50.1		40 MPa
6-CP1	99.9	50.1	✓	
7-CP1	100.0	50.2		20 MPa
7-CP2	99.4	50.1		40 MPa
8-CP1	100.3	50.0		20 MPa

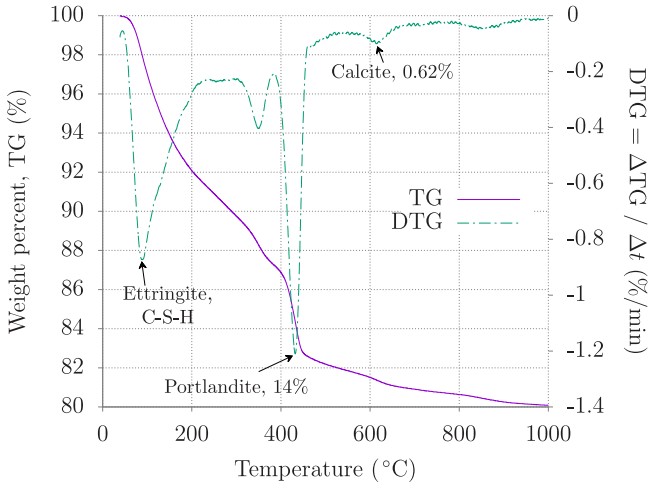

Fig. 4. Thermogravimetric analyses for two material samples of cement collected as part of the coring program.

configured at 40 kV and 25 μA. The diffraction patterns for both samples are shown in Fig. 5, where good repeatability is observed across the two samples. The peaks in the diffraction patterns correspond to the main hydrated phases of early-age cement. The presence of alite, ettringite, tobermorite and belite show that the hydration process was still on-going in the cement, albeit at an advanced stage. The high portlandite content indicated by both TGA and XRD suggests a low rate of carbonation, which also agrees with the low calcite concentration. These observations suggest that the material composition of the cement samples corresponded to that of relatively young cement, exhibiting little or no material degradation.

4. Initial characterization of core plugs

4.1. Ultrasonic measurements

Prior to mechanical testing, all core plugs were subjected to ultrasonic testing, a method that can be used to detect features such as fractures or fissures in the material. The p-wave velocity tests were conducted using a New England Research (NER) equipment controlled by an Autolab 6.0a software and equipped with a Tektronix TDS 3012C oscilloscope. The sensor frequency was 100 MHz, sample frequency was 1.25 GS/s and timing precision of 4 ns/div–10 s/div. Moreover, 32 traces were averaged to create the waveform.

Fig. 6 presents example wave responses for three core plugs retrieved from different positions along the test assembly. The wave form

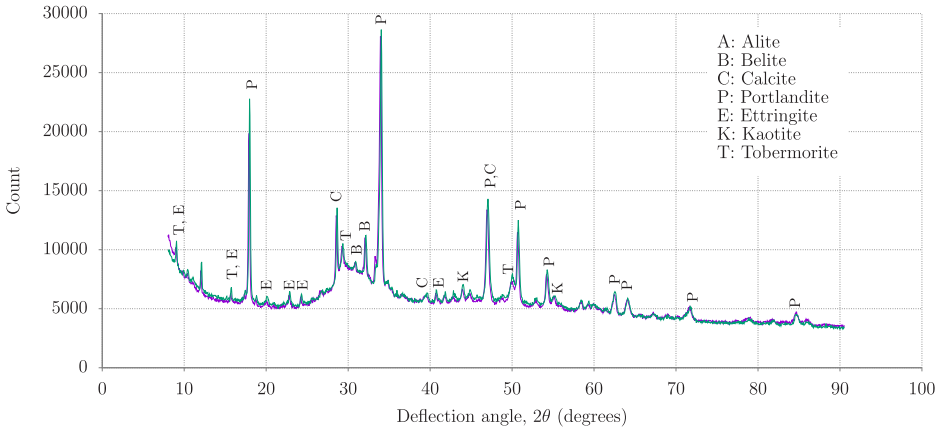

Fig. 5. X-ray diffraction response showing the identification of cement phase peaks for deflection angles 2θ between 8° and 90°.

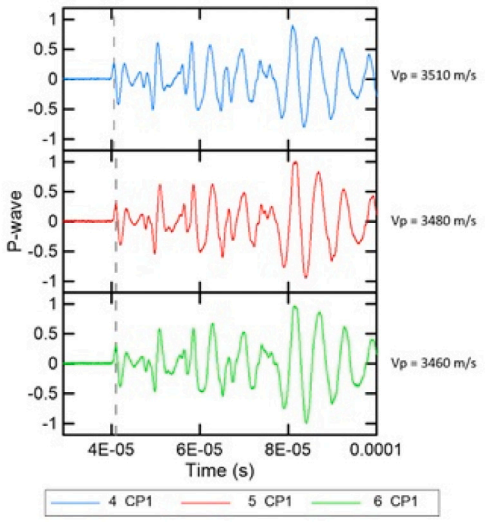

Fig. 6. Example of ultrasonic pulse velocity response for cores 4-CP1, 5-CP1 and 6-CP1.

Fig. 7. Oil well cement paste specimen placed between X-ray source and detector.

Table 3
Ultrasonic p-wave velocity and transit time for the core plugs in Table 2.

Core	P-wave velocity (m/s)	Transit time (10^{-4} s)
1-CP1	3461	1.44
1-CP2	3440	1.45
2-CP1	3489	1.43
3-CP1	3467	1.44
4-CP1	3510	1.43
4-CP2	3488	1.44
5-CP1	3480	1.44
5-CP2	3457	1.45
6-CP1	3460	1.47
7-CP1	3482	1.44
7-CP2	3438	1.46
8-CP1	3476	1.43

and characteristics such as first arrival and attenuation are seen to be similar for these cores. Results of p-wave and transit time for all the cores are presented in Table 3, and we note that the acoustic velocities listed in Table 2 are in the upper range of the interval 3000–3400 m/s specified for early-age neat Class G by Nelson and Guillot (2006).

4.2. Micro-CT imaging

To further probe the internal structure of the cement paste, three specimens, 9-CP1, 9-CP2 and 9-CP3, were scanned using X-ray micro-computed tomography (micro-CT). A Zeiss-Xradia 510 Versa was used for the scans, and the scanning conditions were as follows: 160 kV voltage, 0.4X objective lens (macro lens), and 1601 projection images at 1.1 s exposure time, leading to a total scan time of around 5 h per specimen. Fig. 7 shows a cement sample between the X-ray source and detector. Following reconstruction with a typical filtered back-projection method, approximately 2160 slices with 1024 by 1024 pixels were obtained, with a voxel volume of 45.1 μm^3. An edge-preserving filter called non-local means, available as a FIJI plugin, was applied in order to reduce image noise, as presented in Fig. 8. Segmentation is a step in image processing and analysis in which a region of interest (ROI) is distinguished from the rest of the image, in this case pores and flaws in the cement. Pores and flaws appear as the darkest voxels in the image since they make up the least dense phase of the material. The segmentation process is done by thresholding, where the threshold defines the cut-off in the gray-value range of the image voxel intensity histogram for each ROI. Table 4 shows the void fraction obtained for the three specimens analyzed.

The specimens are seen to be highly uniform with very little identified void volume. As shown in Fig. 3a and as discussed above, the cement cores were all retrieved from inside the inner 7-in tubing, where a wiper ball was used to separate cement slurry from the in-situ spacer fluid during placement of cement. Since the samples appear highly uniform and with little or no flaws, there was likely very

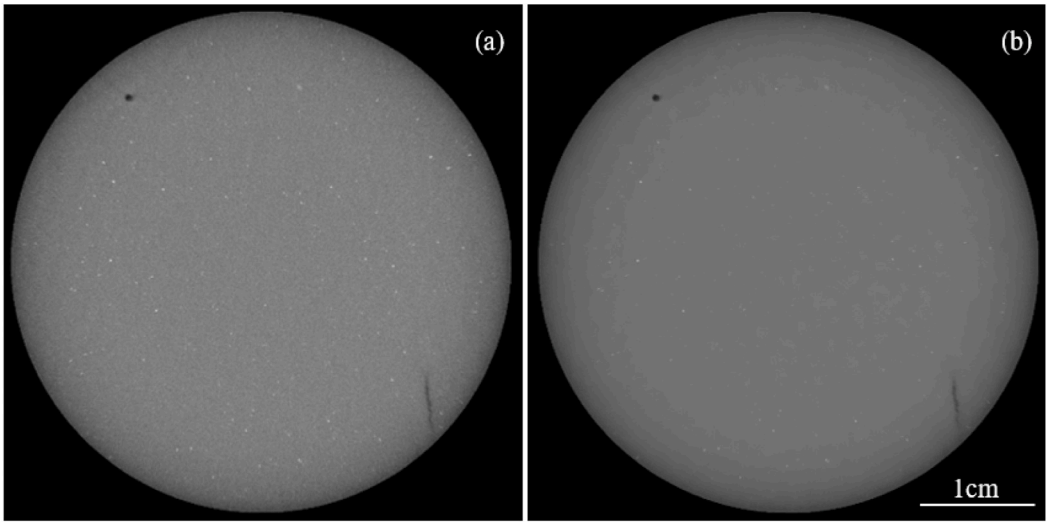

Fig. 8. (a) Slice of 9-CP1 scan and (b) the same slice with a non-local means filter applied.

Table 4
Results of micro-computed tomography analysis.

Core plug	Analyzed volume (mm^3)	Detected void volume (mm^3)	Detected voids fraction (%)
9-CP1	100 682.3	17.5	0.0174
9-CP2	107 524.2	6.9	0.0064
9-CP3	101 827.6	1.2	0.0012

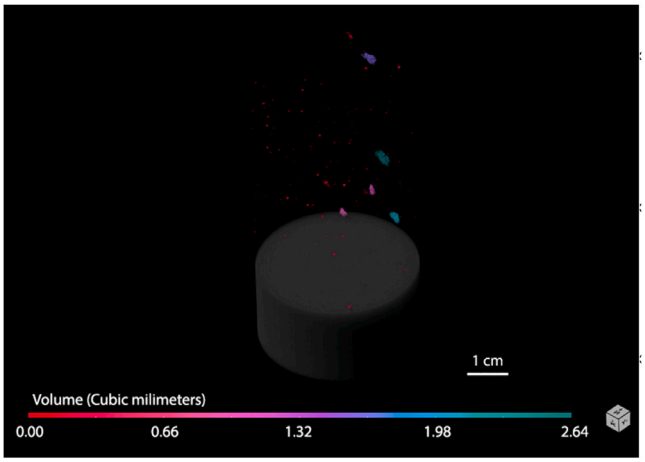

Fig. 9. Three-dimensional reconstruction of sample 9-CP1 with projection of bulk cement paste and voids.

limited contamination of cement by the spacer fluid. The cement cores are therefore considered representative of hardened cement with no significant traces of contamination by other well fluids (see Fig. 9).

5. Mechanical testing

The machine used for mechanical testing of the cores was a MTS triaxial testing system model 815 with a compression load capacity of 2700 kN and a confining pressure capacity of 80 MPa, equipped with a MTS flex test 60 controller. For the unconfined compression tests, a two-step procedure was adopted. The first step was controlled by the axial extensometer with deformation at a strain rate of 0.00005 s^{-1} until the axial load reached 40 kN (about 40% of the material strength in UCS tests). The second step was controlled by the circumferential displacement of the sample at a strain rate of 0.00005 s^{-1} until failure was detected.

For the confined tests, the triaxial cell vessel was closed and then filled with Mobil Mobiltherm 605 fluid. Prior to testing, all specimens went through a rigorous preparation process, where self-fusing silicone electrical tape and a heat-shrinkable FEP membrane were used (Fig. 10a). Two axial and one circumferential extensometer were also connected to the cores before commencing the mechanical test, see Fig. 10b. The heat-shrinkable membrane was used to prevent direct contact between confining fluid and the test specimen, thereby preventing potential damage to the specimen that could have affected its behavior. After filling the triaxial cell, the confining pressure was applied at a rate of 2 MPa/min to the pre-defined values of 10, 20 or 40 MPa. The subsequent test protocol was the same as that used for the unconfined tests. Three samples were prepared and tested under each of the three confining pressures 10, 20 and 40 MPa. The mechanical tests were performed with the cores in their original condition, following coring from the cemented test sections. The tests were performed under undrained conditions, where pore fluid would not escape the cores. For porous and weak material in particular, drained or undrained conditions may affect the mechanical strength of the specimen. Due to these specimens appearing uniform and not visibly degraded, it was assumed that the specific test condition would not significantly influence the strength measurements.

6. Results

6.1. Uniaxial compressive strength testing

As specified in Table 2, three cement paste cores were selected for uniaxial or unconfined compression tests. The recorded axial stress as function of axial strain (positive), ε_1, and lateral strain (negative), ε_3, is shown in Fig. 11, where also the average linear elastic Young's modulus has been estimated from the measurements below axial strains of 0.2%. Note that here, and in the remainder of the study, we adopt the rock mechanics sign convention where compressive stresses and compressive strains are positive.

The three cores display very similar linear elastic responses with an average Young's modulus of 14.9 GPa based on the initial stress

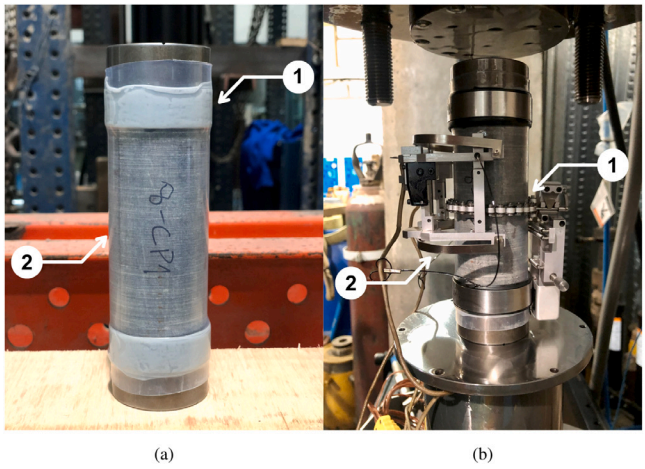

Fig. 10. Specimen preparation process: (a) the ∅ 50 mm × 100 mm cylindrical specimen with the self-fusing silicone electrical tape (1) and heat shrinkable FEP membrane (2) and (b) specimen positioned in the MTS triaxial testing machine with the circumferential (1) and axial (2) extensometers.

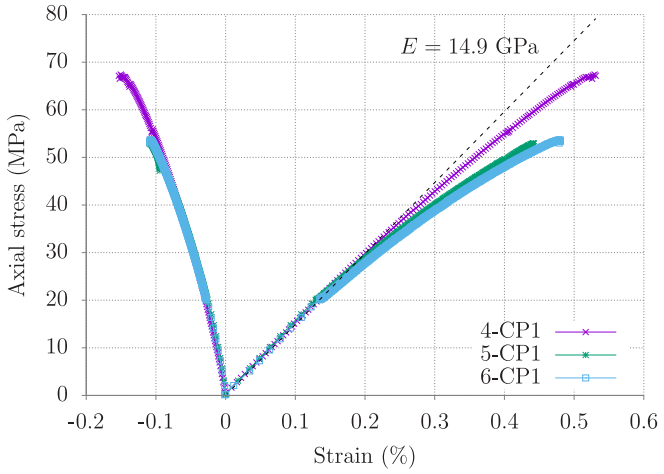

Fig. 11. Measurements of axial and lateral strains for increasing axial stress in the unconfined, uniaxial compression tests. The compressive, axial strain is positive while the tensile, lateral strain is negative.

response. This value is close to that found by *e.g.* Jimenez et al. (2019) and Li et al. (2019). Deviations from the initial linear behavior is observed starting from approximately 0.2% axial strain, or some 30 MPa axial stress. The unconfined compressive strength is found to vary from 53 MPa to 67.4 MPa, with an average of approximately 58 MPa. These values are of equal magnitude and similar to those previously reported by Li et al. (2019) and also by Thiercelin et al. (1998). In all three cases, the compressive shear failure is abrupt and follows a stage of nonlinear stress–strain behavior, as seen in Fig. 11.

Fig. 12 shows the axial strain as function of the measured volumetric strain for the unconfined tests in Fig. 11. Here and in the following, the volumetric strain is defined as $\varepsilon_{vol} = \varepsilon_1 + 2\varepsilon_3$. The cores fail at axial strains of approximately 0.45–0.5% with a corresponding volumetric strain in excess of 0.2%. The relatively small strain carrying capacity in the absence of confinement is anticipated and expected for cement pastes. In Fig. 12, we also fit a linear curve to the lower strain and linear elastic regime. Since the Poisson ratio is defined as the ratio of lateral to axial strains, $\nu = -\varepsilon_3/\varepsilon_1$, it is expected that the volumetric and axial strains be related by $\varepsilon_{vol} = (1 - 2\nu)\varepsilon_1$ under ideal elastic loading conditions. Therefore one may estimate Poisson's ratio from the slope of the linear curve. The Poisson's ratio was estimated as $\nu \approx 0.21$

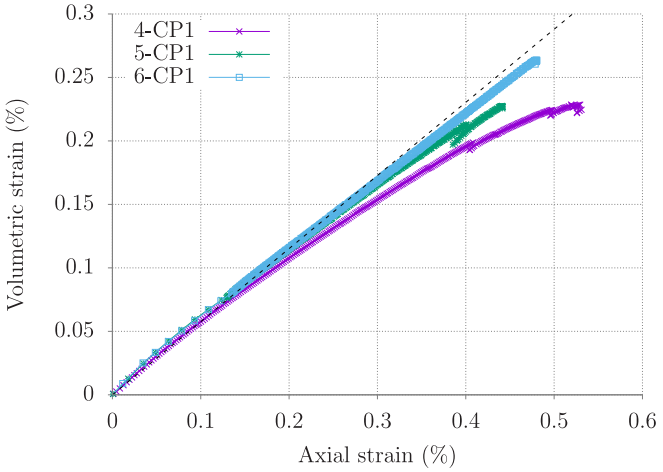

Fig. 12. Axial and volumetric strain for the unconfined tests. The dashed line corresponds to $\varepsilon_{vol} = (1 - 2\nu)\varepsilon_1$ with $\nu = 0.21$.

based on the three tested unconfined specimens. This value is similar to those reported by Li et al. (2019).

6.2. Triaxial compressive tests

The stress–strain measurements acquired under different confining pressures are provided in Fig. 13, where also the unconfined measurements are repeated for comparison. The tests performed with a confining pressure all show a significant strain hardening phase prior to reaching the ultimate deviatoric stress. While the unconfined samples failed at axial strain of approximately 0.5%, a significant increase in the strain at the ultimate deviatoric stress is now observed. Interestingly, the ultimate deviatoric stress is seen to be approximately 80 MPa for all tests performed with a confining pressure. That is, no significant frictional strengthening is observed with increasing confining pressure. Further, while all cement paste samples tested at unconfined conditions experienced clear shear failure, none of the samples at 10 MPa confining pressures or higher did so. The stress–strain curves instead show a prolonged plastic phase with apparently no loss of load-carrying capacity up to the point of termination of the test. The measurements generally suggest very good reproducibility.

The dashed straight lines in Fig. 13 once again indicate the estimated Young's modulus from the early phase of the tests, and we now observe a weakly decreasing value with increasing confining pressures; we estimate Young's moduli of respectively 13.8 GPa, 12.8 GPa and 11.1 GPa at confining pressures of 10 MPa, 20 MPa and 40 MPa. Combined with the unconfined estimate of 14.9 GPa, we conclude that increasing confining pressure leads to a decrease in Young's modulus in these samples.

Plots of axial and volumetric strains are shown in Fig. 14. Measurements up to an axial strain of 1% were used as a basis for determining the Poisson ratios. Compared to 0.21 in the unconfined case, the values were here calculated as 0.19, 0.17 and 0.1 at confining pressures of 10, 20 and 40 MPa, respectively. Thus, and as per the Young's modulus, the Poisson ratio is found to decrease with increasing confining pressures. It is further noted that the samples undergo volumetric compression throughout most of the loading. Only at the highest confining pressure tested did the cement paste exhibit a weakly dilating stage past the ultimate deviatoric stress before the test was terminated. Further, plots of the deviatoric stress as function of volumetric strain is shown in Fig. 15 for measurements at 10, 20 and 40 MPa confining pressure. As seen from these plots, the samples appear to deform more easily at higher confining pressures so that the volumetric strain at a given deviatoric stress increases with increasing confining pressure. These

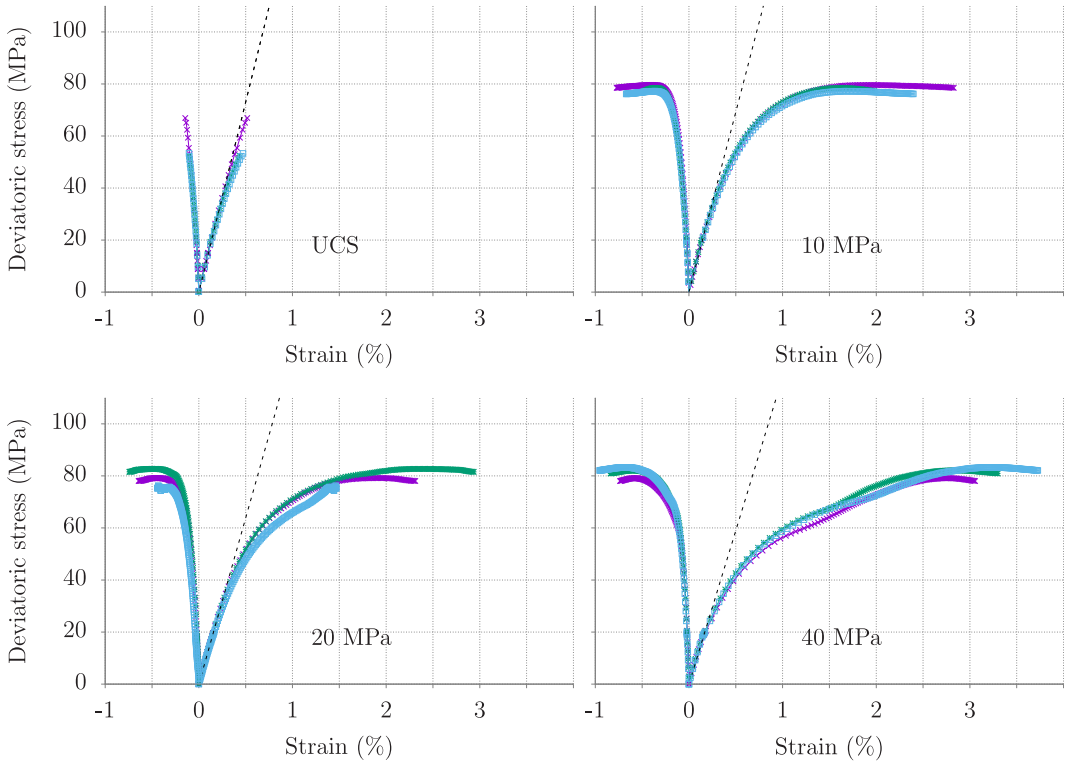

Fig. 13. Measurements of axial and lateral strains for increasing deviatoric stresses at unconfined conditions (UCS) and at three different confining pressures. The stress–strain curves are terminated after the ultimate deviatoric stress when the stress decreases to 98.5% of the maximum value. As detailed in Table 2 and as seen in the figure, three cores have been tested at each level of confining pressure.

observations suggest an increased softening or ductility of the cement as the confining pressure increases, reflected both in the reducing Young's modulus and the increasing volumetric strain.

As discussed by *e.g.* Paterson and Wong (2005), brittle-to-ductile transitions at low temperatures involve a combination of cataclastic flow mechanisms and crystal plasticity. Cataclastic flow describes permanent material deformation by fracturing of the material into fragments and the relative movement of the fragments. This deformation is pressure-sensitive due to the normal force that acts between fragments and determines the sliding friction. Depending on the initial porosity of the material, cataclastic flow can be associated with either dilatancy or a net compaction (Paterson and Wong, 2005). The other main deformation mechanism, crystal plasticity, is associated with permanent deformation within the grains of the material. The deformation is essentially volume-preserving and independent of the confining pressure (Paterson and Wong, 2005). In the study by Sakai et al. (2016), the ultimate deviatoric stresses at 30 MPa and 100 MPa confining pressure tended toward the same stress level, similar to our observations in Fig. 13. This observation was attributed to crystal plasticity and that the plastic strength of cement hydrates limited the deviatoric stress at these confining pressures (Sakai et al., 2016). Turning to the results presented above, Fig. 15 shows a pronounced compaction of the samples, most likely due to shear-enhanced compaction of pores in the cement. Based on the results of the micro-CT scans, the cement cores have a low concentration of macropores and no detectable flaws. The volumetric strain observed in Fig. 15 is therefore mainly attributed to a combination of elastic compression of the cement matrix and compaction of small gel pores and capillary pores that are not identified in the micro-CT images. For the reasons mentioned above, *i.e.* no significant pressure-sensitivity in the ultimate deviatoric stress, and a net compaction throughout the test cycle, the observed brittle-to-ductile transition in Fig. 13 does not easily categorize as either cataclastic flow or purely crystal plastic deformation. Consequently, further work is required to better explain the mechanisms behind the transition from brittle to ductile behavior observed in these cement paste samples.

6.3. Current study limitations and uncertainty

It should be pointed out that the cement specimens used for the above measurements were cured at surface, and that mechanical tests were done at room temperature. These conditions may have affected mechanical properties of the cores tested in this study, and causing the quantitative stress–strain curves presented above to differ from actual downhole behavior of the same cement system. Further, the core material was all sourced from the cement inside the inner tubing, and both visual inspections and the micro-CT scans indicate no visible contamination of the cores by the water-based spacer fluid that originally occupied the test sections. Thus, the current results apply to neat and homogeneous cement cores with few or no intrusions of foreign material. Finally, and as pointed out in Section 2, the cemented test cells were sectioned into shorter segments at the end of the cementing operation and stored uncovered outside, exposed to local weather conditions. While chemical characterization of the cement by TGA and XRD did not reveal any obvious alterations to the composition of the hardened cement, storage conditions could still affect the mechanical properties of the cement over time. We consider these as the most relevant sources of uncertainty when comparing results presented in this study and actual downhole behavior.

7. Stress–strain model for confined well cement

The transition observed in Fig. 13, from a maximum deviatoric stress of $\sigma_{ucs} \approx 58$ MPa at unconfined conditions, to an ultimate deviatoric stress of approximately 80 MPa under confining conditions, suggests an empirical model of the form

$$\sigma_1 - \sigma_3 = \sigma_{ucs} + \frac{a\sigma_3}{1 + a\sigma_3}(b - \sigma_{ucs}) \quad (1)$$

for the ultimate deviatoric stress. Here σ_3 is the confining pressure, σ_{ucs} is the uniaxial compressive strength, and σ_1 is the largest principal

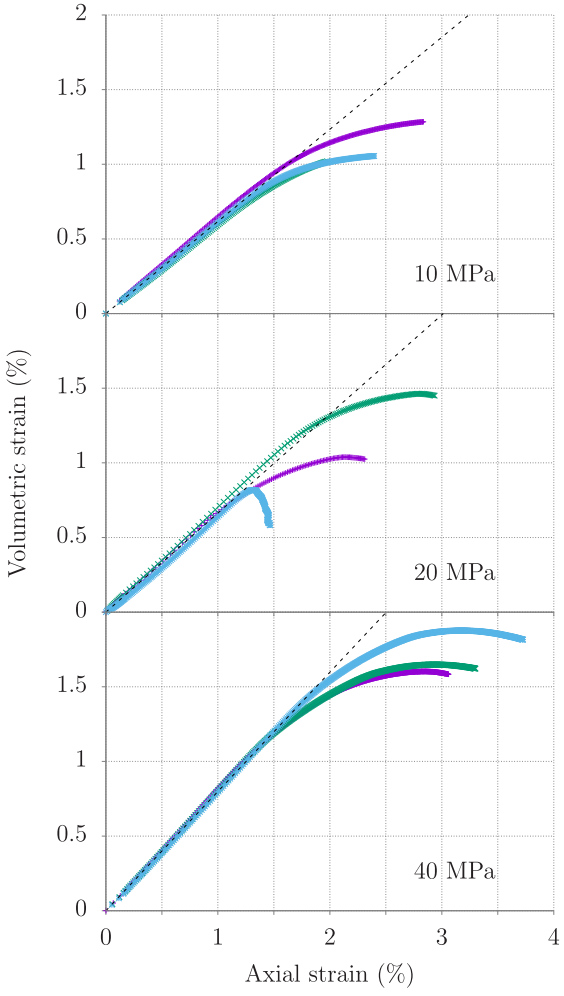

Fig. 14. Axial and volumetric strains measured at different confining pressures. Note that the volumetric strain is here measured relative to the start of the deviatoric loading phase.

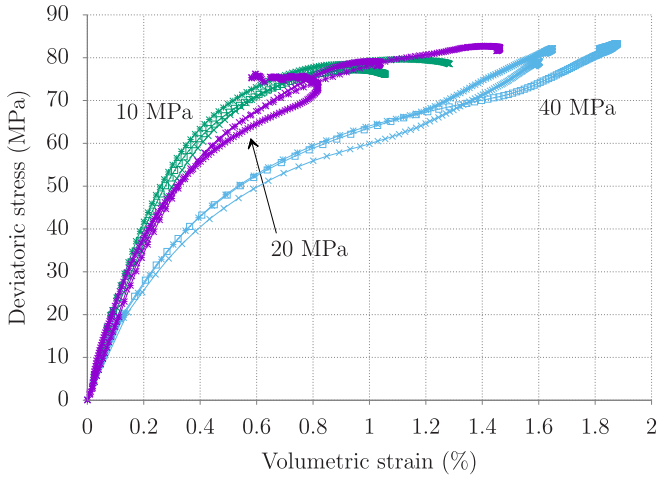

Fig. 15. Volumetric strain for samples tested under confining pressure. Note that the volumetric strain is here measured relative to the start of the deviatoric loading phase.

stress, taken as the sum of the applied axial stress and the confining pressure. The two fitting parameters a and b describe respectively the transition region toward the asymptotic strength value, and the value

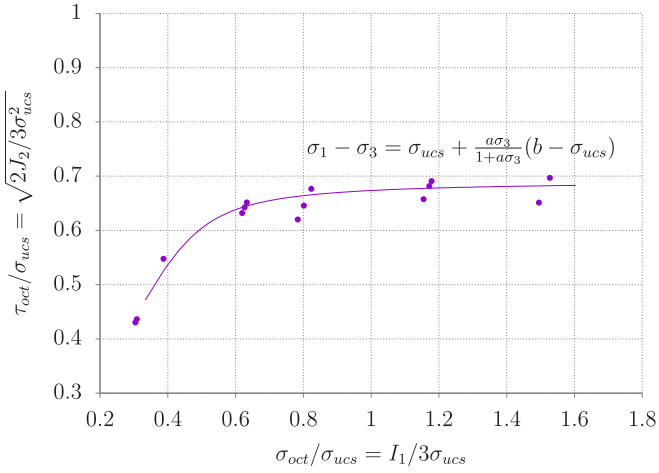

Fig. 16. Plot of the unconfined and confined strength measurements in terms of the normalized octahedral normal and shear stresses. The solid line is the least squares fit of the empirical relation in Eq. (1) with $a = 0.36$ MPa^{-1} and $b = 84.15$ MPa.

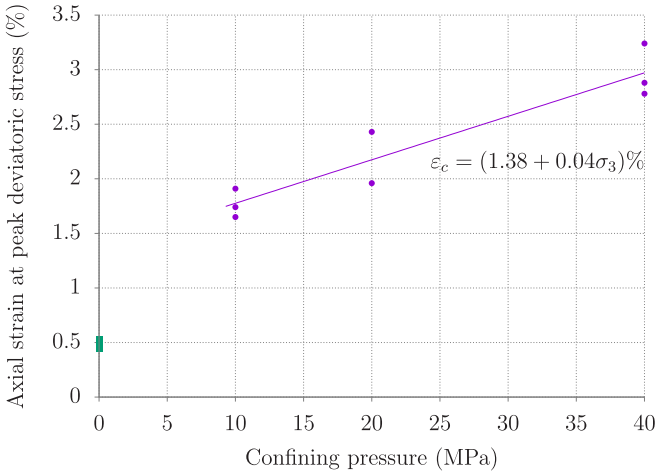

Fig. 17. Variation of axial strain at ultimate deviatoric stress with confining pressure. The axial strain at failure for the unconfined test samples are also indicated in the figure.

of the asymptotic ultimate deviatoric stress. To fit the equation to our measurements, we take $\sigma_{ucs} = 58$ MPa based on the average UCS values and we fit a and b by minimizing the squared residuals between model and measurements. The best fit corresponds to $b = 84.15$ MPa and $a = 0.36$ MPa^{-1}. The result is illustrated by the solid line in Fig. 16, where the points correspond to the uniaxial and triaxial measurements presented above. In the figure, the ultimate deviatoric stress is plotted as function of the octahedral mean and shear stresses, σ_{oct} and τ_{oct}, respectively. These are defined through the stress invariants $I_1 = \sigma_1 + \sigma_2 + \sigma_3$ and $J_2 = \left[(\sigma_1 - \sigma_2)^2 + (\sigma_1 - \sigma_3)^2 + (\sigma_2 - \sigma_3)^2\right]/6$ as $\sigma_{oct} = I_1/3$ and $\tau_{oct} = \sqrt{2J_2/3}$.

The proposed empirical correlation is seen to capture the transition from the lower deviatoric strength at unconfined conditions, corresponding to the measurements at the lowest octahedral mean stress, to the plateau in ultimate deviatoric stress when subjected to confining pressure.

Further, when it comes to the axial strain that corresponds to the ultimate deviatoric stress, ε_c, we plot results for both unconfined and confined conditions in Fig. 17. The solid line is a linear curve fit to the measurements at 10 MPa and higher confining pressures, given by $\varepsilon_c = (1.38 + 0.04\sigma_3)\%$, with σ_3 the confining pressure.

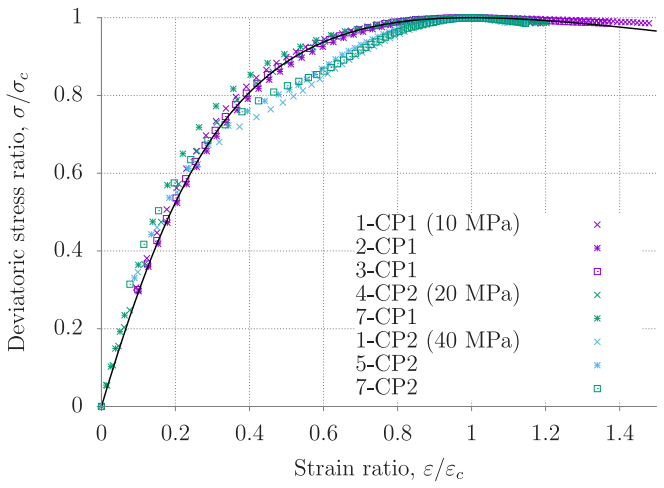

Fig. 18. Stress–strain measurements for all tests with a confining pressure. The deviatoric stress is here normalized by the ultimate deviatoric stresses, σ_c, while the strain is normalized by the strain at ultimate deviatoric stress, ε_c. The solid line corresponds to the nonlinear stress–strain model in Eq. (2) with $r = 1.5$.

Next, by normalizing the stress–strain measurements to the ultimate deviatoric stress under confinement, $\sigma_c \approx 80$ MPa, and to the axial strain corresponding to the ultimate deviatoric stress level, ε_c, the measurements collapse toward a single curve, as shown in Fig. 18. The solid line in the figure is the nonlinear stress–strain model proposed by (Popovics, 1973):

$$\frac{\sigma}{\sigma_c} = \frac{xr}{r - 1 + x^r}, \tag{2}$$

where σ denotes the deviatoric stress, and $x = \varepsilon/\varepsilon_c$ is the ratio of axial strain ε to the strain at the ultimate stress ε_c, and $r = (1 - \sigma_c/(\varepsilon_c E))^{-1}$ where E is the unconfined Young's modulus, set to 14.9 GPa based on the data in Fig. 11. The least squares fit to seven data sets gives a value of $r = 1.5$, corresponding to the solid line in Fig. 18. The collapse of the measurements onto this single curve suggests that the relatively simple constitutive Eq. (2) can be used to model the confined stress and strain behavior of the well cement studied herein. Finally, from the definition of r, it is observed that for these data sets, $\sigma_c/\varepsilon_c = E_{sec} \approx E/3$, or $n = E/E_{sec} \approx 3$, where E_{sec} is the secant modulus at the ultimate deviatoric stress. The same range for n is suggested for instance for mortars with ultimate deviatoric stress of approximately 76 MPa (Popovics, 1973), which is similar to the ultimate level in most of our confinement tests.

Thus, to conclude this section, the normalized confined stress–strain measurements are considered to be well-represented by the nonlinear model in Eq. (2), which is a smooth model covering the initial elastic phase to the ultimate deviatoric stress and beyond. To put the model in dimensional form, $\sigma_c \approx 80$ MPa for the current cement samples at confined conditions, while the results in Fig. 17 can be used to approximate ε_c for different confining pressures.

8. Summary and conclusions

The mechanical behavior and ultimate deviatoric strength of oil well cement pastes under confining pressures up to 40 MPa were studied. The samples were cored from test sections that had been cemented with an oil well cement slurry prepared in a full-scale offshore batch mixer. Initial characterization of core plugs using acoustic measurements, chemical analyses and micro-CT scans show small variations in bulk properties. Unconfined cement samples are found to exhibit linear elastic behavior up to axial strain of approximately 0.2% with an average Young's modulus of 14.9 GPa and Poisson ratio of 0.21. At larger strains, the stress–strain response deviates from the initial slope, terminating with brittle shear failure at axial strains of approximately 0.5%. The corresponding average uniaxial compressive strength is 58 MPa.

Confining pressure resulted in markedly different stress–strain behavior, as expected. At confining pressures of 10 MPa or higher, the cement paste samples exhibited a deviatoric stress plateau and continued plastic deformation with no apparent loss in load-carrying capacity. The magnitude of the peak deviatoric stress reached a level of approximately 80 MPa for all samples tested under confining pressures greater than 10 MPa and up to 40 MPa. Increased confining pressure was found to also reduce the Young's modulus and the Poisson ratio of the cement, suggesting an effectively softer response at higher confining pressure. Finally, our results suggest the confined stress–strain behavior of well cement can be parameterized by the simple, normalized Eq. (2) that can be implemented into numerical simulations of well cement under relevant confined conditions.

While cements are generally brittle while unconfined, we observe a distinct transition toward ductile and softer response under confinement. The more ductile and flexible response of well cement under relevant confining pressures is considered to be a positive characteristic of cement as a barrier material for zonal isolation. In fact, new casing expansion technologies developed for treating annular migration paths and sustained-casing pressure problems rely on the capacity of confined annular cement to sustain significant mechanical strains without failing. An important result of this study, namely that the confined stress–strain behavior of well cement can be described by a simple dimensionless equation, can be used for numerical modeling of cement behavior under downhole conditions. Future work will seek to further explore effects of confinement on cement behavior within the framework of poromechanics and will include effects of porosity and long-term loading.

CRediT authorship contribution statement

Victor Nogueira Lima: Methodology, Investigation. **Flávio de Andrade Silva:** Conceptualization, Supervision. **Hans Joakim Skadsem:** Conceptualization, Formal analysis, Writing – original draft, Funding acquisition. **Katherine Beltrán-Jiménez:** Methodology, Resources, Investigation. **Jonas Kristoffer Sunde:** Methodology, Investigation.

Declaration of competing interest

The authors declare that they have no known competing financial interests or personal relationships that could have appeared to influence the work reported in this paper.

Acknowledgments

The Research Council of Norway, the Petroleum Safety Authority Norway, AkerBP, ConocoPhillips, Petrobras, Shell and Total are acknowledged for financing the work through PETROMAKS2 project number 308767/E30 and the P&A Innovation Program — a program for accelerating P&A technology development. The construction of the cemented test sections used as basis for the current study was financed by the Research Council of Norway, ConocoPhillips, AkerBP, Equinor, and Wintershall through PETROMAKS2 project number 244577 and the research centre DrillWell – Drilling and Well Centre for Improved Recovery, a research cooperation between NORCE, NTNU, SINTEF, and UiS.

References

Arjomand, E., Bennett, T., 2018. Effect of curing conditions on the mechanical properties of cement class G with the application to wellbore integrity. Aust. J. Civ. Eng. 16, 143–157. http://dx.doi.org/10.1080/14488353.2018.1519985.

Bittleston, S.H., Ferguson, J., Frigaard, I.A., 2002. Mud removal and cement placement during primary cementing of an oil well – Laminar non-Newtonian displacements in an eccentric annular Hele-Shaw cell. J. Eng. Math. 43, 229–253. http://dx.doi.org/10.1023/A:1020370417367.

Bittleston, S., Guillot, D., 1991. Mud removal: Research improves traditional cementing guidelines. Oilfield Rev. 44–54.

Bois, A.P., Garnier, A., Rodot, F., Saint-Marc, J., Aimard, N., 2011. How to prevent loss of zonal isolation through a comprehensive analysis of microannulus formation. SPE Drill. Complet. 26, 13–31. http://dx.doi.org/10.2118/124719-PA.

Bourissai, M., Meftah, F., Brusselle-Dupend, N., Lecolier, É., Bonnet, G., 2013. Evolution of the elastic properties of an oilwell cement paste at very early age under downhole conditions: Characterization and modelling. Oil Gas Sci. Technol. - Rev. IFP Energ. Nouv. 68, 595–612. http://dx.doi.org/10.2516/ogst/2012087.

Cornelissen, E.K., 2019. Method for sealing cavities in or adjacent to a cured cement sheath surrounding a well casing. US 2019/0264547 A1.

Du, H., Guo, R., Radonjic, M., 2015. Microstructure and micromechanics of wellbore cements under compression and thermal loading. In: U.S. Rock Mechanics/Geomechanics Symposium. pp. 1–11, ARMA-2015-498.

Eseme, E., Urai, J., Littke, R., Krooss, B., 2007. Review of mechanical properties of oil shales: Implications for exploitation and basin modelling. Oil Shale 24.

Ghabezloo, S., Sulem, J., Guédon, S., Martineau, F., Saint-Marc, J., 2008. Poromechanical behaviour of hardened cement paste under isotropic loading. Cem. Concr. Res. 38, 1424–1437. http://dx.doi.org/10.1016/j.cemconres.2008.06.007.

Handin, J., 1965. Strength of oil well cements at downhole pressure-temperature conditions. SPE J. 5, 341–347. http://dx.doi.org/10.2118/1300-PA.

Handin, J., Hager, Jr., R.V., 1957. Experimental deformation of sedimentary rocks under confining pressure: Tests at room temperature on dry samples. AAPG Bull. 41, 1–50.

Handin, J., Hager, Jr., R.V., 1958. Experimental deformation of sedimentary rocks under confining pressure: Tests at high temperature. AAPG Bull. 42, 2892–2934.

Handin, J., Hager, Jr., R.V., Friedman, M., Feather, J.N., 1963. Experimental deformation of sedimentary rocks under confining pressure: Pore pressure tests. AAPG Bull. 47, 717–755.

Jennings, H.M., Thomas, J.J., Rothstein, D., Chen, J.J., 2002. Cements as Porous Materials. John Wiley & Sons, Ltd., pp. 2971–3028. http://dx.doi.org/10.1002/9783527618286.ch40, chapter 6.11.

Jimenez, W.C., Darbe, R., Pang, X., 2019. Enhanced mechanical-integrity characterization of oilwell annular sealants under in-situ downhole conditions. SPE J. 24, 2308–2319. http://dx.doi.org/10.2118/185341-PA.

Kupresan, D., Heathman, J., Radonjic, M., 2014. Casing expansion as a promising solution for microannular gas migration. SPE Drill. Complet. 29, 366–371. http://dx.doi.org/10.2118/168056-PA.

Le Saout, G., Lécolier, E., Rivereau, A., Zanni, H., 2006. Chemical structure of cement aged at normal and elevated temperatures and pressures: Part i. class g oilwell cement. Cem. Concr. Res. 36, 71–78. http://dx.doi.org/10.1016/j.cemconres.2004.09.018.

Li, Y., Lu, Y., Ahmed, R., Han, B., Jin, Y., 2019. Nonlinear stress-strain model for confined well cement. Materials 12, 2626. http://dx.doi.org/10.3390/ma12162626, 1–15.

Nelson, E.B., Guillot, D. (Eds.), 2006. Well Cementing, second ed. Schlumberger, Sugar Land, Texas, US.

Palou, M.T., Šoukal, F., Boháč, M., Šiler, P., Ifka, T., Živica, V., 2014. Performance of G-oil well cement exposed to elevated hydrothermal curing conditions. J. Therm. Anal. Calorim. 118, 865–874. http://dx.doi.org/10.1007/s10973-014-3917-x.

Patel, H., Salehi, S., 2019. Development of an advanced finite element model and parametric study to evaluate cement sheath barrier. J. Energy Resour. Technol. 141, 092902. http://dx.doi.org/10.1115/1.4043137.

Paterson, M.S., Wong, T.F., 2005. Experimental Rock Deformation - The Brittle Field. Springer-Verlag, Berlin Heidelberg.

Popovics, S., 1973. A numerical approach to the complete stress–strain curve of concrete. Cem. Concr. Res. 3, 583–599. http://dx.doi.org/10.1016/0008-8846(73)90096-3.

Radonjic, M., Kupresan, D., Du, H., Olabode, A., 2015. Microstructures and micromechanics of wellbore cement under compression. In: The 13th International Congress on Rock Mechanics. pp. 1–12.

Sakai, Y., Nakatani, M., Takeuchi, A., Omorai, Y., Kishii, T., 2016. Mechanical behavior of cement paste and alterations of hydrates under high-pressure triaxial testing. J. Adv. Concr. Technol. 14, 1–12. http://dx.doi.org/10.3151/jact.14.1.

Skadsem, H.J., Kragset, S., Sørbø, 2019. Cementing an irregular annulus geometry: full-scale experiments and 3D simulations. In: SPE/IADC International Drilling Conference and Exhibition. The Hague, The Netherlands, 2019, pp. 1–15. http://dx.doi.org/10.2118/194091-MS. SPE/IADC 194091.

Thiercelin, M., Baumgarte, C., Guillot, D., 1998. A soil mechanics approach to predict cement sheath behavior. In: SPE/ISRM Rock Mechanics in Petroleum Engineering. Trondheim, Norway, 1998, pp. 1–9. http://dx.doi.org/10.2118/47375-MS. SPE 47375.

Wolterbeek, T.K., Cornelissen, E.K., Nolan, S., Todea, F., Stam, W., Roggeband, S.M., Dam, L., van Riet, E.J., Ruckert, F., Keultjes, W.J.G., 2021. Restoration of annular zonal isolation using localized casing expansion (LCE) technology: A proof of concept based on laboratory studies and field trial results. J. Pet. Sci. Eng. 197, 108103. http://dx.doi.org/10.1016/j.petrol.2020.108103, 1–28.